Steady and unsteady regimes in a T-shaped micro-mixer: synergic experimental and numerical investigation

Alessandro Mariotti, Chiara Galletti[1], Roberto Mauri, Maria Vittoria Salvetti, Elisabetta Brunazzi

Dipartimento di Ingegneria Civile e Industriale, University of Pisa, Pisa, Italy

Abstract

Despite the very simple geometry, T-shaped micro-mixers are characterized by different flow regimes when operated for liquid mixing. In this work, experiments and direct numerical simulations are employed jointly to investigate such flow regimes. First, a novel methodology is proposed to provide a quantitative comparison with numerical predictions starting from simple flow visualization experiments that use non-collimated light. This method is applied and validated in the steady flow regimes. Moreover, flow visualizations provide for the first time an experimental support to the flow dynamics scenarios for the periodic unsteady flow regimes previously proposed in the literature on the basis of numerical simulations. In particular, at a Reynolds number, based on the bulk velocity and on the hydraulic diameter of the mixing channel, of approximately 225, the flow passes from the steady engulfment regime into an unsteady asymmetric regime, which is characterized by a periodic dynamics of the three-dimensional structures present in the mixer. In this regime, the flow in the mixing channel always remains asymmetric promoting, thus, the mixing between the two streams. By further increasing the Reynolds number, another change in flow dynamics is observed. In the new regime, called periodic symmet-

[1]corresponging author

ric regime, the flow always maintains a double mirror symmetry in the mixing channel and this leads to a dramatic decrease of mixing. The flow unsteadiness is mainly due to a periodic shift of the vortical structures in the top part of the mixer along the direction parallel to the incoming flow.
Keywords: flow visualization, micro-reactor, T-junction, Computational Fluid Dynamics, Direct Numerical Simulations

---

1. Introduction

Mixing and reaction in small devices have been found to be very appealing and effective for different chemical engineering applications [1] [2]. Micro-mixers and micro-reactors, constituted by micro-channels of width ≤ 1 mm, in which reactants are fed through inlet branches and mix, offer continuous operation and high heat transfer capacity due to the very high surface to volume ratio. Hence, such micro-devices appear well suited for all chemical and biochemical transformations that benefit of enhanced mixing and heat transfer in a well controlled residence time. Examples are fast reactions, whose yield may be improved through an optimal control of mixing, or highly exothermic reactions, which benefit of a better heat transfer, or hazardous reactions, which can be carried out in small volumes. In comparison to conventional batch processes (e.g. mechanically agitated vessels) microdevices can be thus operated with lower dilution, leading to higher yield and lower environmental impact. Indeed, continuous processing has been indicated recently as one of the main "Key Green Engineering Areas for Sustainable Manufacturing" by the American Chemical Society, the Green Chemistry Institute and several global pharmaceutical corporations [3], different specific drivers to implement continuous operations were also highlighted for several individual cases [4]. Recently, the possibility and advantages of carrying out continuous flow synthesis of active pharmaceutical ingredients in micro-reactors has been shown even for heterogeneous conditions

occurring in the Buchwald-Hartwig arylamination reaction [5] [6].
Moreover, the scale-up procedures of the synthetic route and process from laboratory on gram, or even milligram, scale to ton and multi-ton scale, that are hardly to be derived in conventional batch or semi-batch processes, are straightforward [7] or completely avoided in micro-rectors, as the required production rate is simply obtained by a numbering-up of the reactors often assembled in modular systems [8].
The main difficulty is that the flow is laminar, so mixing should be promoted by a clever design of the microdevice [9]. The simplest configuration is provided by a T-mixer in which the inlet channel axis is perpendicular to that of the main channel. This micro-mixer is suited to carry out fundamental studies; moreover it is often found as junction element in more complex micro-mixer networks.

Despite the very simple geometry, the laminar hydrodynamics in a T-shaped micro-mixer is really complex. In particular, mixing in such device has been largely investigated when the working fluid is water at the same conditions and flow rates from the two inlets. Different flow regimes have been identified as a function of the mixing channel Reynolds number, i.e. $Re = \rho U d/\mu$. Here d is the mixing channel hydraulic diameter, U is the inlet bulk velocity, ρ and μ are the fluid density and dynamic viscosity, respectively. These flow regimes have been classified into *steady regimes*, at low Re, namely the stratified, steady symmetric (vortex), steady asymmetric (engulfment) regimes, and *unsteady regimes*, namely the periodic asymmetric, periodic symmetric and chaotic ones.

At very low Re, in the stratified regime, the inlet streams flow side by side through the mixing channel, resulting in a completely segregated pattern. Increasing Re, in the vortex regime, a double pair of counter-rotating vortical structures are originated at the confluence region. The vortical structures in the mixing channels show four legs of equal strength. Since the flow in the

vortical regime preserves the geometrical reflectional symmetries, the two inlet streams remain segregated and mixing occurs only through diffusion. Increasing Re, a tilting of the vortical structures at the top of the mixer is observed, which leads to a symmetry breaking. Consequently, the two legs of each vortex entering in the outflow channel are not equal in terms of intensity. Moving towards the end of the outflow channel, the weakest couple of legs disappears and only two co-rotating vortical structures survive. A sudden increase of the degree of mixing is associated with such transition, so that many efforts in the literature have been devoted at predicting the critical Re at which this transition occurs and understanding its dependence on geometric parameters ([10] [11], [12], [13]) and fluid properties ([14] [12]).

The above steady regimes have been deeply investigated using both experimental and numerical techniques. Measurements are mainly based on advanced optical techniques as micro-Particle Image Velocimetry ($\mu-$PIV) and micro-Laser Induced Fluorescence (μ-IF) (e.g. [15] [16] [17] [18]) that allow to investigate sections of the mixer by using laser sheets. The numerical modeling is carried out through Computational Fluid Dynamics (CFD, e.g.[19]) that in some case has been combined with stability analysis ([10]) to stem light into the mechanisms promoting the symmetry breaking driving the onset of the engulfment regime.

For further increased Re, the flow was found to become unsteady, but well periodic. The unsteady periodic flow regimes were mainly investigated through numerical simulations [20] [21] [11] [22] [23] [24]. The only experimental investigation, to our knowledge, is the one described in [25] and [26], carried out in a rather large mixer (depth $H = 20$ mm) with square inlet cross sections by means of LIF. In particular, in [25] and [26], two different periodic regimes were distinguished. In the first one, occurring at lower Re, Thomas et al. [25] [26],

observed two or four vortical structures periodically forming at the T-channel junction, which they attributed to the roll-up of the shear layers present in this zone. This regime is asymmetric (asymmetric periodic regime) and it is characterized by a high degree of mixing. By further increasing Re, the flow was found to remain unsteady, but characterized by a symmetric four-vortex topology (symmetric periodic regime), leading to a detrimental effect of mixing. Both the unsteady periodic regimes were analyzed in details in [11] and [21] through numerical simulations in terms of the dynamics of three dimensional vortical structures.

Experimental flow visualizations of the same T-mixer configuration are presented and compared herein to numerical predictions. A novel method is introduced, which may provide a quantitative comparison between experiments and numerical simulations, when only simple flow visualizations are available. This method is firstly applied and validated in the well documented steady flow regimes. Then, flow visualization experiments were carried out to study the unsteady regimes and support the flow dynamic scenarios predicted by direct numerical simulations.

List of Symbols

A	absorbance of the solution, [-]
$\mathbf{A}$	anti-symmetric part of the non-dimensional velocity gradient, [-]
C	dye concentration, [mol m^{-3}]
d	mixing channel hydraulic diameter, [m]
D	dye molecular diffusivity, [m^2 s^{-1}]
H	height of the T mixer, [m]
I	light intensity, [W m^{-2}]
$\mathbf{L}$	symmetric tensor $\mathbf{L} = \mathbf{S} \cdot \mathbf{S} + \mathbf{A} \cdot \mathbf{A}$, [-]
L_i	length of the inlet channel, [m]
L_o	length of the mixing channel, [m]
m	proportionality constant between A and C, [m^3 mol^{-1}]
N	order of the Lagrange polynomial interpolants, [-]
P	modified non-dimensional pressure, [-]
Pe	Peclet number, [-]
Re	Reynolds number, [-]
$\mathbf{S}$	symmetric part of the non-dimensional velocity gradient, [-]
Sc	Schmidt number, [-]
St	Strouhal number, [-]
t	time, [s]
U	inlet bulk velocity, [m s^{-1}]
$\mathbf{u}$	non-dimensional velocity vector, [-]
W_i	width of inlet channel, [m]
W_o	width of mixing channel, [m]
x, y, z	spatial coordinates, [m]
X, Y, Z	non-dimensional spatial coordinates, [-]

Greek symbols

λ_2	second largest eigenvalue of the tensor $\mathbf{L}$, [s^{-2}]
μ	dynamic viscosity, [kg m^{-1} s^{-1}]
θ	non-dimensional time, [-]
ρ	fluid density, [kg m^{-3}]
τ	characteristic period of the flow dynamics, [s]
ϕ	normalized dye mass fraction, [-]

2. Experiments

2.1. T-mixer geometry

The experimental model is made of polymethylmethacrylate (PMMA) and consists of three layers: a central layer containing a T-shaped cutting through, a top and bottom layer for optical access and fluidic connections. The central layer has a thickness of 1 mm, while the thickness of the top and bottom layers is equal to 3 mm. The three layers are bond with screws and two double-sided (Nitto-Denko, 597A-597AP) adhesive films.

A sketch of the T-mixer geometry is shown in Figure 1a, together with the adopted frame of reference. The inlet channels have a square cross section, with $W_i = H = 1$ mm, while the mixing channel presents a $2:1$ aspect ratio, i.e. $W_o = 2H = 2$ mm, so that its hydraulic diameter is $d = 4H/3$. The length of the inlet channels, $L_i = 40$ mm$\approx 30d$ is enough to allow a fully developed flow at the confluence while the length of the mixing channel [11], $L_o = 60$ mm $\approx 45d$, is enough to allow the complete evolution of vortical structures.

[Figure 1 about here.]

2.2. Experimental set up

The mixer inlets are fed with deionized water streams by using a KD Scientific syringe pump Gemini 88, equipped with two Becton Dickson plastic syringes of 60 ml. The two streams were introduced at equal flow rates. A sketch of the experimental apparatus is shown in Figure 1(b). The mixing of the streams inside the T-mixer was observed with an upright microscope (model Eclipse 80i from Nikon, Japan) with a magnifying lens of $4\times$ and an aperture value setting equal to $N.A. = 0.13$. The light source is a D-LH 12V-100W halogen lamp and all the experiments were performed in a dark room in order to maintain a constant level of luminosity with time and to minimize any reflections and shadows. The images were collected by using the high-speed camera Optomotive Velociraptor HS, having a square monochrome sensor with a resolution of 2048×2048 pixels. The maximum frame rate of the camera is equal to 174 frames/s for the whole sensor, which can be increased by activating only a smaller rectangular portion of the sensor (the frame rate is inversely proportional to the number of pixel in the horizontal direction). Thus, for the investigated flow regimes, a resolution of 920×2048 pixels and a frame rate up to 387 frames/s are chosen. After preliminary studies, the sampling frequency of 387 frames/s is such to avoid aliasing problems at the higher Reynolds numbers. The exposure time of each image is equal to $\delta T = 10^{-6}$ s, thus three orders of magnitude smaller than the sampling frequency.

The investigated region is equal to $1.8d \times 4d$ and includes the T-mixer junction and the initial segment of the mixing channel. A $0.5\times$ lens had to be mounted in front of the high-speed camera to capture the whole region in a single image. As for the steady regimes, the same region is also obtained by merging multiple images of smaller T-mixer portions, acquired without the $0.5\times$ lens, and thus having a double resolution (the presented figures of the steady regimes have a

resolution of 1840×4096 pixels).

In order to differentiate the two streams and visualize the mixing process, one inlet stream is colored with a food colorant, Ponceau 4R dye (also denoted by E number E124) (Sigma-Aldrich), dissolved with concentration of $1.9 \cdot 10^{-3}$ M. Such concentration is so low that it does not alter the fluid properties, that are practically those of deionized water. The E124 dye, when dissolved, yields a dark color solution, which becomes grey in the monochromatic recorded images.

2.3. Image acquisition and analysis

The attenuation of the light crossing the dyed solution is often assumed to obey the Lambert-Beer's law stating that the absorbance is linear with the concentration (see 27). We investigated, first, if the linear relationship holds also with our experimental set up and operating conditions. We filled the mixer with various sample solutions of known levels of dye concentration and we acquired images for all these solutions. The resulting light-intensity image of each set was analyzed pixel by pixel to calculate the relationship of light absorbance with concentration for every individual pixel in the image.

For each (i, j)-th pixel, the analysis of the light absorbance vs. the concentration, showed a Lambert-Beer-type relationship:

$$ln\left(\frac{I_{blank,ij}}{I_{k,ij}}\right) = A_{k,ij} = m_{ij}C_k \tag{1}$$

where $I_{blank,ij}$ is the light intensity of the blank solution (the solution with zero dye content), $I_{k,ij}$ the light intensity of the k-th solution with dye concentration C_k, m_{ij} is a constant of proportionality and $A_{k,ij}$ is the absorbance of the k-th solution. As an example, the results for some pixels randomly distributed over

the frame are reported in Figure 2(a). They almost all lye on straight lines.

Pixel intensities can further be converted into normalized absorbances according to the following relationship:

$$\frac{ln(I_{blank,ij}) - ln(I_{k,ij})}{ln(I_{blank,ij}) - ln(I_{max,ij})} = \frac{A_{k,ij}}{A_{0,ij}} = \frac{C_k}{C_0} \tag{2}$$

where $A_{0,ij}$ and $I_{max,ij}$ are the maximum absorbance and light intensity, respectively, of the solution with the highest dye concentration, C_0. The parity plot in Figure 2(b) shows the averaged normalized measured absorbance value vs. the real (a-priori known) normalized concentration. The normalized absorbance is reported in terms of average value over the image, plus and minus its standard deviation, which is always very low, i.e. less than 0.02. The relationship between the normalized absorbance and the normalized real concentration is of course also linear for all the pixels and Equation (2) is satisfied.

[Figure 2 about here.]

In the experimental flow visualizations, images were processed with Matlab® to convert pixel intensity maps into normalized concentration maps as illustrated in the scheme of Figure 3. The procedure was fully automatized and off-line. It required, thus for each set of experiments the acquisition first of the references $I_{blank,ij}$ and $I_{max,ij}$, obtained by feeding the mixer only with the blank and $1.9 \cdot 10^{-3}$ M dye solution, respectively, before using the two streams together. In order to limit the uncertainty related to time fluctuation of pixel intensity, the reference $I_{blank,ij}$ and $I_{max,ij}$ are chosen to be their arithmetic mean values over 100 frames each.

[Figure 3 about here.]

Light intensity images were then converted into normalized dye concentration images, according to Equation (2), where, obviously, in this case $I_{k,ij} = I_{ij}$

and $C_k = C_{ij}$, being I_{ij} and C_{ij} the instantaneous values of light intensity and dye concentration, respectively, in the (i, j)-th pixel.

In order to prevent any kind of hysteresis in the mixing process, the pump was stopped after each run, before changing the flow rate settings to reach the desired Reynolds number, and started again. To avoid transient effects, images were acquired once the flow regime was established. Moreover the reproducibility of the experiment was always assessed: several frames were acquired for the steady regimes, checking their consistency, and many flow periods were recorded for the unsteady regimes.

3. Direct Numerical Simulations

3.1. Governing equations

The liquid motion is described by the unsteady incompressible non-dimensional form of the Navier-Stokes equations:

$$\nabla \cdot \mathbf{u} = 0 \tag{3}$$

$$\frac{\partial \mathbf{u}}{\partial \theta} + \mathbf{u} \cdot \nabla \mathbf{u} = -\nabla P + \frac{1}{Re} \nabla^2 \mathbf{u} \tag{4}$$

where length, velocities and time are normalized with the mixing channel hydraulic diameter d, the inlet bulk velocity U and the convective time d/U. P is the modified non-dimensional pressure. These equations are coupled with a conservation equation which governs the dye dynamics:

$$\frac{\partial \phi}{\partial \theta} + \mathbf{u} \cdot \nabla \phi = \frac{1}{Pe} \nabla^2 \phi, \tag{5}$$

where ϕ is the dye mass fraction and $Pe = Ud/D$ is the Peclet number, with D denoting the dye molecular diffusivity. It is worth noting that for liquids

the Schmidt number is very large, i.e. $Sc = \mu/(\rho D) = O(10^3 \div 10^4)$, so that $Pe = ScRe = O(10^6)$.

3.2. Numerical solvers

Simulations were performed with two different CFD codes: the commercial finite-volume code Fluent by ANSYS® and the open-source spectral-element code NEK5000 [28]. In particular, the former code was mainly used for the characterization of the steady regimes, whereas the latter for the unsteady ones. Although the numerics is very different, the agreement between the two codes for the simulation of micro-mixers is excellent, as reported in [29].

As for the Fluent simulations, a fully structured grid with $4.7 \cdot 10^6$ cells was employed. Specifically, the cells are cubical at the confluence regions and elongate towards the inlets and the outlet. In a cross section of the mixing channel there are 40×80 elements. The Schmidt number was set to $Sc = 5000$ corresponding to the diffusivity of the dye employed in the experiments. A steady solver with a second order discretization scheme was employed, with a SIMPLE algorithm to handle the pressure-velocity coupling. At convergence the normalized residuals for velocities did not change with iterations and most of the times fell below $1 \cdot 10^{-11}$ [30]. The steadiness of the solution was also checked by monitoring velocity and concentration values in some locations in the mixing channel at different iterations. As mentioned above, the concentration field was discretized using the same mesh size as for the velocity field; an extended discussion to justify this assumption was presented in [31]. C++ subroutines were implemented in the code to allow the visualization of the vortical structures.

The NEK5000 code was employed to carry out efficiently unsteady simulations as it is massively parallelized. The code is based on the spectral-element method. The spatial discretization consists of hexahedral elements and the velocity space is spanned by Nth-order Lagrange polynomial interpolants, based

on tensor-product arrays of Gauss-Lobatto-Legendre (GLL) quadrature points in each spectral element. Time discretization was handled with a third order backward differential formula (BDF3). The diffusive terms are treated implicitly, while a third order explicit extrapolation (EXT3) is considered for the convective terms. The computational domain consists of a structured grid with 12250 spectral elements, with 5×10 elements uniformly distributed in a cross section of the mixing channel. The polynomial order N for the velocity is fixed to 7, while an order of 5 is imposed for the pressure,thus using the common P_N/P_{N-2} scheme, for a total of about $4 \cdot 10^6$ degrees of freedom for each velocity component. As for time discretization, the explicit extrapolation for the convective terms in the BDF3-EXT3 scheme enforces a small time-step, i.e. of $7.0 \cdot 10^{-4}$, corresponding to a CFL number ≤ 0.3. This computational set up is the same as that used in the simulations in [11]. However, a scalar equation was added to predict the dye concentration; for this equation, stability issues forced to use a rather low Sc number, i.s. $Sc = O(100)$ as in [21]. However the NEK5000 simulations refer to the high Re range (unsteady regimes), so that the diffusive transport is negligible compared to the convective one. Moreover, for the area of the T-mixer under investigation, i.e. near the confluence region up to $Y = -3$, such diffusion has not time to occur. The simulations were run in order to capture at least 20 periodic cycles after discarding the initial transient.

The equations reported in Section 3.1 are solved in both codes using no-slip velocity and no-mass-flux at the channel walls, and uniform velocity and concentration at the entrance. As mentioned before, the inlet channels are long enough to provide a fully developed flow at the T confluence. A pressure outlet condition with ambient pressure was imposed with Fluent at the exit, while free outflow conditions (i.e., $\frac{\partial u_x}{\partial y} = 0$, $P - \frac{1}{Re}\frac{\partial u_y}{\partial y} = 0$ and $\frac{\partial u_z}{\partial y} = 0$) were set for the simulations carried out with NEK5000.

The numerical simulations were all initialized using uniform, non-developed, conditions, i.e. solutions obtained with Re numbers close to the investigated one were not used to speed up the simulations. This was made to avoid any kind of hysteresis that could be present near critical Reynolds numbers corresponding to a change of regime [11][12].

3.3. Post-processing of numerical results

In order to validate the numerical model, the predicted data were post-processed on purpose with a Matlab® routine to emulate the flow visualization experiments, by keeping in mind that such images result from the light attenuation through the fluid, that depends on the dye concentration. Basically, the numerically predicted concentration distribution across the mixer is collected and averaged over the mixer depth (i.e., along the z coordinate) in order to compare it with experimental images. In this manner the local CFD information was used to reconstruct field information as that available from the experiments (see Figure 3). Such methodology allows to use experimental data that are obtained with a simple light (instead of more sophisticated laser) for the quantitative validation of numerical models.

4. Results

The experimental and numerical outcomes are preliminary validated in the well-known steady regimes (Section 4.1). Subsequently, the unsteady regimes are analyzed; experimental flow visualizations are again compared with the results obtained through direct numerical simulations (Section 4.2). In the following figures, all coordinates are made non-dimensional by using the mixing channel hydraulic diameter, i.e. $X = x/d$, $Y = y/d$ and $Z = z/d$. The local dye concentration is normalized by the inlet concentration so that it goes from 0 to 1.

4.1. Steady regimes

Figures 4(a) and 4(b) compare the experimental flow visualization at $Re = 50$ with that obtained by the post-processing of CFD passive scalar concentration field. The regime appears well segregated in both pictures, showing no mixing in the channel except for a little dye diffusion. The vortical structures, computed from the numerical velocity field through the λ_2-criterion [32], are shown in Figure 4(c). According to this criterion, a vortex is defined as a connected fluid region where the second largest eigenvalue of the symmetric tensor $\mathbf{L} = \mathbf{S} \cdot \mathbf{S} + \mathbf{A} \cdot \mathbf{A}$ is negative, i.e. $\lambda_2 < 0$. $\mathbf{S}$ and $\mathbf{A}$ indicate the symmetric and anti-symmetric part of the velocity gradient, that are the strain rate and vorticity tensors, respectively, i.e. $\nabla \mathbf{u} = \mathbf{S} + \mathbf{A}$. The isosurface of λ_2 in Figure 4(c) is 3D; for ease of comparison, the same 2D view as for the dye field visualizations is shown in the bottom panel, while a top view is provided in the top panel.

[Figure 4 about here.]

The quantitative comparison between experiments and CFD is provided in Figure 5. Here the dye concentration is reported as a function of the X coordinate at different Y locations in the mixing channel. It can be observed that the experimental and predicted concentration gradients are well in agreement. It is worth remarking that the experimental concentration comes from the image analysis, hence stems from a global view, whereas the CFD concentration comes from the average of local concentration values over the channel depth. For the sake of clarity, the numerical distribution of the dye concentration in the corresponding cross sections is also reported. In the present vortex regime, the dye concentration is obviously uniform in the Z direction.

[Figure 5 about here.]

By increasing the Reynolds number, the two streams remain segregated

despite three-dimensional vortical structures form, as shown in Figure 6 at $Re = 120$. The top parts of these structures originate from the flow recirculations occurring near the top wall of the mixer at the confluence of the two streams entering the inlet channels [10]. The so-generated vortical structures are convected in the mixing channel, forming two pairs of counter-rotating *legs* for each vortical structure. For low Reynolds numbers, as in Figure 6, the flow and the described vortices preserve the two reflectional geometrical symmetries and, thus, the two streams remain segregated and mixing occurs only through diffusion.

[Figure 6 about here.]

The experimental and numerical dye concentrations are reported for the engulfment regime in Figures 7(a) and 7(b), at $Re = 160$. Here the flow patterns appear more complex, however at first glance we can notice the very good agreement between experiments and predictions. The corresponding vortical structures, found in numerical simulations and identified as previously through the λ_2 criterion, are shown in Figure 7(c). Although the view in Figures 7(a) and 7(b) is an averaged one, it can offer an insight into the main flow features, described in previous works (e.g. [10]). At the top of the mixer, two recirculation bubbles, generated from the confluence, are observed. In the engulfment regime, such bubbles are tilted in the $X - Z$ plane, so that in the global view provided by the dye concentration images they appear a bit superimposed. Two counter-rotating vortical structures originate in these recirculation regions near the top walls of the mixer, which correspond to the top parts of the vortical structures shown in Figure 7(c). The so-generated vortices are convected by the stream into the outflow channel, forming two legs for each vortical structure (see again Figure 7(c)). Due to the tilting of the separation bubbles on the top wall, each of the two vortices generated in the bubbles is asymmetric, i.e. the two

legs of each vortex entering in the outflow channel are not equal in terms of intensity, shape, and position. Moving towards the end of the outflow channel, the weakest couple of legs disappears (see [10] for a more detailed description). As previously said, the signature of these complex vorticity structures can be identified in the dye concentration fields. At $Y = -0.15$ and $Y = -0.45$ the complex patterns come from the two strong and the two weak legs, while the latter almost vanish at $Y = -1.3$, and completely disappear at $Y = -2.4$, where the concentration is affected by the presence of only two main co-rotating vortices. The signature of the vortex legs can also be seen in the numerical dye concentration distribution in the $X - Z$ cross sections shown at different Y in the top panels of Figure 8. As well documented in the literature, the flow asymmetry in the engulfment regimes significantly increases the mixing compared to the segregated and vortical regimes. This can be clearly seen by observing the left-hand region of Figures 7(a) and (b) and of the top panels of Figure 8. Even though the left inlet corresponds to no dye (white), a black zone is present near the left wall; such zone is due to the presence of dye that is pushed there by the velocity field induced by the vortical structures previously described and, in particular, by the two co-rotating strong vortex legs. Same observations hold for the right-hand side of each figure. In the bottom panels of Figure 8, quantitative comparison between average experimental and CFD concentration is reported at different Y coordinates in the mixing channel. A general very good matching can be noticed. The concentration gradient in the center of the channel is well captured along with concentration peaks and valleys that are due to the vortices convecting the dye. Some discrepancies are found near the walls, where the experimental concentration may be affected by minor geometrical irregularities of the experimental device.

[Figure 7 about here.]

[Figure 8 about here.]

The same quantities as in the previous analysis at $Re = 160$ are shown at higher Re ($Re = 200$), still in the steady engulfment regime, in Figures 9 and 10, in order to investigate possible effects of increasing the Reynolds number. If we compare Figure 7 and Figure 9, for the higher Reynolds number we can notice at the top of the mixer apparently a single (instead of a double) recirculation bubble. However, this is due to a larger tilting angle of the top parts of the vortical structures (see Figure 9(c)), which leads to a superimposition of such recirculation regions in the view adopted in Figures 9(a) and 9(b). Moreover, we can observe that the dye field pattern in the mixing channel is different for the two Reynolds numbers. In both cases, there is a region near the channel axis in which the two streams appear to be segregated, because this zone is little affected by the mixing induced by the vortical legs. At $Re = 160$ such region firstly enlarges and than slightly restricts, but it persists until the end of the visualization frame, whereas at $Re = 200$ the restriction is more evident and the segregated region near the axis almost disappears at the end of the visualization frame. This is due to the fact that the co-rotating stronger vortical legs are more intense and more swirled at $Re = 200$ (compare Figures 7(c) and 9(c)), leading thus to a more efficient mixing. The quantitative comparison between experimental and numerical averaged concentration is reported in Figure 10 (bottom panels). Again the agreement is generally satisfactory. However, at $Re = 200$, beside the main concentration gradient near the channel axis, some local peaks are found in the experimental concentration distribution, which are not captured in numerical simulations. These peaks are due to the fact that in the vortex legs one stream is trapped into the other in a spiraling concentration distribution, leading to local maxima or minima of the average dye concentration when averaging at different X locations. The signatures of these peaks are

visible also in Figure 9(a) in the form of the concentration streaks present in the downstream part of the mixing channel. In the numerical simulations, probably due to numerical diffusion, the spiraling concentration pattern is less sharp than in experiments (see the top panels of Figure 10) and, thus, the local peaks are smoothed out. Consistently, no streaks are visible in Figure 9(b). The presence of streaks was also previously observed experimentally by [33] who argued that they may be due to the formation of fluid filaments during the engulfment. Instead, Mouheb et al. [17] attributed the streaks to some pulsations of their syringe-type pump, that they state can occur for $Re < 150$, so for lower Re than the ones observed here. In the present investigation fluctuations could be hardly noticed for very low Re ($Re < 20$), not even reported here, whereas the behavior was perfectly steady at the higher Re shown above.

[Figure 9 about here.]

[Figure 10 about here.]

4.2. Unsteady regimes

As previously discussed in the Introduction, further increasing Re, the flow is expected to become unsteady and periodic. In the present experiments and simulations, at $Re = 220$ the flow was observed to be perfectly steady, whereas at $Re = 225$ it was characterized by periodic unsteady motions. Figure 11 reports experimental and CFD snapshots of the average dye concentration at $Re = 280$ for different equally spaced instants t within a characteristic period of the flow dynamics, τ, corresponding to a Strouhal number $St = \frac{d}{U\tau}$=0.218. The initial time is arbitrary since the flow is periodic. For a better interpretation, the vortical structures identified by the λ_2 analysis are also reported. As mentioned previously the experimental image resolution is lower than that of the steady case, because for the unsteady regimes the investigation region corresponded

to the whole image. First of all, the experimental and the CFD images show an extremely good matching at all instants. At $\frac{t}{\tau} = 0$ the vortical structures and the flow visualizations are similar to those of the steady engulfment regime at $Re = 200$ (see Figure 9). The most important difference is that the top part of the vortical structures are more tilted and are closer than in the steady engulfment regime. Indeed, as observed in [21] and [11], during the cycle, the top parts of the vortical structures tend to approach each other, and as they become closer, their tilting angle increases. This difference in the top part of the vorticity field is hard to be detected from the flow visualizations; a possible signature is the fact that the flow recirculation, present in between the top vortex parts in the steady engulfment regime, is no more visible in the left and center panels of Figure 11(a). Another difference, whose signature is visible also in the flow visualizations (compare the left and center panels of Figure 11(a) with Figures 9(a) and (b)), is that, at the considered time instant, the downstream part of the vortex legs is more swirled than in the steady engulfment regime. The reason of this difference will be explained later. Subsequently, at $\frac{t}{\tau} = 0.25$, the two vortical structures have merged: the top parts, containing vorticity of different sign, rapidly annihilate, while the two strong legs form a vorticity blob, clearly visible in the center of the right bottom panel of Figure 11(b). In the meanwhile, the top parts of two new structures start to form from both sides of the Y axis. This complex dynamics is hardly detectable from flow visualizations, although in the upper part they are significantly different from those of the previous instant and of the steady engulfment regime. Later on the vorticity blob is convected toward the exit of the mixing channel. The passage of the blob causes the twisting and deformation of the legs of the vortices; this is visible in the region $-0.75 > Y > -1.5$ in the right bottom panel of Figure 11(c) at $\frac{t}{\tau} = 0.5$ and more downstream in the right bottom panel of Figure 11(d) at $\frac{t}{\tau} = 0.75$. The

signature of the blob passage is clearly detectable also in the corresponding flow visualizations in the left and center panels of Figures 11(c) and (d). By the way, the twisting of the downstream part of the vortex legs in Figure 11(a) is due to the previous passage of the vorticity blob. While the vorticity blob is convected through the mixing channel, the topology of the new formed vortical structures in the top part of the mixer (right top panels of Figures 11(c) and (d)) become similar to the one in the engulfment regime. The top parts of corresponding flow visualizations also show patterns very similar to those observed in the steady engulfment regime. These new vortical structures eventually undergo the same dynamics starting again the previously described cycle. For a better visualization of the flow dynamics, please see the video at $Re = 280$ provided in the supplementary material. In particular, the experimental flow visualization video is compared with the numerical evolution of the concentration field and the vortical structures.

Summarizing, the vorticity dynamics found in the present numerical simulations is the same as the one described in [11] and in more detail in [21]. Since, the experimental flow visualizations are in very good agreement with the numerical ones, the present experiments support the periodical flow dynamics previously suggested in the literature based on numerical simulations only. Although some of the complex phenomena observed in this regime are hardly detectable from flow visualizations, some relevant features, such as the passage of the vorticity blob and the consequent twisting of the vortex legs, are clearly visible.

[Figure 11 about here.]

[Figure 12 about here.]

Both the findings of numerical simulations in [21, 11] and of the experiments in [25, 26] suggest that further increasing the Reynolds number, another change in the flow dynamics should be expected with the establishment of the so-called

periodic symmetric regime. Consistently, at $Re = 325$ a change in the flow topology and dynamics is observed in both experiments and simulations (until $Re = 320$ the flow resembled that already shown at $Re = 280$). An example of this new dynamics, which persists up to $Re = 510$, is shown in Figure 12 for $Re = 450$. Consistently with the numerical findings in [11] for the same T-mixer geometry, in this regime, the flow in the mixing channel always maintains a double mirror symmetry with four vortex legs, approximately of the same intensity (see the bottom right panels in Figure 12), as in the steady vortex regime. The symmetry in the mixing channel makes the two streams remaining almost segregated, as it can be seen by the flow visualizations in the left and center panels in Figure 12. This obviously leads to a dramatic decrease of mixing in this regime. As observed in [11], most of the flow dynamics takes place in the top part of the mixer and it is characterized by periodic small oscillations of the top parts of the 3D vortical structures in the x direction, as shown in the top right panels of Figure 12. During the oscillations, the tilting angle of the top parts of the 3D vortical structures slightly changes but it remains always very low, thus not enough to break the double symmetry in the mixing channel. This dynamics is periodic with a Strouhal number of $\mathrm{St} = 0.226$. The signature of this dynamics is evident in the experimental and numerical flow visualizations: it can be seen that, when the top parts of the 3D vortical structures are shifted towards the left (negative X values), the flow stream entering from the right penetrates in the left top part of the mixer (left and center panels in Figures 12(a) and (b)). The opposite occurs when the top parts of the 3D vortical structures are shifted towards the right (left and center panels in Figures 12(c) and (d)). A clearer view of the flow dynamics is provided by the video at $Re = 450$ included in the supplementary material, which shows the time evolution of experimental flow visualizations, of dye concentration predictions and of vortical structures.

Thus, also for this regime, the present experiments support the periodical flow dynamics previously suggested in the literature based on numerical simulations only.

Finally, at $Re = 520$ the flow becomes chaotic, with a new increase in mixing. This regime is not shown here for the sake of brevity.

[Figure 13 about here.]

[Figure 14 about here.]

5. Conclusions

A joint experimental and numerical investigation is presented of flow regimes occurring in a T-shaped mixer operating with a single liquid. Experiments are based on rather simple flow visualizations that are performed using a non-collimated light and thus provide a global view of the flow. Direct numerical simulations are carried out by using two different CFD codes. Both experiments and simulations spanned a large range of Reynolds numbers corresponding to different flow regimes, which are summarized in Table 1.

A simple methodology which allows a quantitative comparison to be obtained between numerical predictions and measurements is proposed. The dye concentration field obtained in direct numerical simulations is averaged over the mixer depth to be compared with the experimental visualization images. The methodology was successfully validated in the well-known steady flow regimes, and, in particular, in the engulfment regime. A good agreement between simulations and experiments was found in all cases. Moreover, the signatures of the complex three-dimensional vortical structures present in the mixer in the different regimes, and available only in the simulations, could be identified in both experimental and numerical flow visualizations.

Finally, flow visualizations allow an experimental support to be given for the first time to the flow dynamics scenarios previously proposed in the literature, on the basis of numerical simulations, for the unsteady flow regimes occurring at higher Reynolds numbers. In particular at $225 \leq Re \leq 320$ the flow presents periodic motions that are characterized by a large degree of asymmetry in the mixing channel and, thus, by a high degree of mixing (Table 1). Although some details of the complex vorticity dynamics, observed in this regime in numerical simulations, are hardly detectable from flow visualizations, the main features, such as the passage of a vorticity blob in the mixing channel and the consequent twisting of the vortex legs, are clearly visible. Then, at $325 \leq Re \leq 510$, although still unsteady and periodic, the flow is always characterized by a double mirror symmetry in the mixing channel, which largely hampers the degree of mixing (Table 1). The flow unsteadiness is mainly due to the periodical shift of the vortical structures in the top part of the mixer along the direction parallel to the incoming flow. The signatures of this periodic motion are clearly visible in the experimental and numerical flow visualizations.

[Table 1 about here.]

6. Acknowledgments

This work was supported by the University of Pisa through the "Progetti di Ricerca di Ateneo PRA 2017-2018" funding program. The authors wish also to thank CINECA computing center (Bologna, Italy) for allowance of computational resources under ISCRA program (class B project "MIMIC"). Moreover the authors are grateful to Tommaso Andreussi, Deborah Spaltro, Tommaso Pannuzi and Cesare Merello.

References

[1] V. Hessel, H. Löwe, F. Schönfeld, Micromixers-a review on passive and active mixing principles, Chemical Engineering Science 60 (2005) 2479 – 2501.

[2] I. Rossetti, M. Compagnoni, Chemical reaction engineering, process design and scale-up issues at the frontier of synthesis: Flow chemistry, Chemical Engineering Journal 296 (2016) 56 – 70.

[3] C. Jiménez-González, P. Poechlauer, Q. B. Broxterman, B.-S. Yang, D. am Ende, J. Baird, C. Bertsch, R. E. Hannah, P. Dell'Orco, H. Noorman, S. Yee, R. Reintjens, A. Wells, V. Massonneau, J. Manley, Key green engineering research areas for sustainable manufacturing: A perspective from pharmaceutical and fine chemicals manufacturers, Organic Process Research & Development 15 (2011) 900–911.

[4] P. Poechlauer, J. Colberg, E. Fisher, M. Jansen, M. D. Johnson, S. G. Koenig, M. Lawler, T. Laporte, J. Manley, B. Martin, A. OKearney-McMullan, Pharmaceutical roundtable study demonstrates the value of continuous manufacturing in the design of greener processes, Organic Process Research & Development 17 (2013) 1472–1478.

[5] A. Pommella, G. Tomaiuolo, A. Chartoire, S. Caserta, G. Toscano, S. P. Nolan, S. Guido, Palladium-n-heterocyclic carbene (nhc) catalyzed cn bond formation in a continuous flow microreactor. effect of process parameters and comparison with batch operation, Chemical Engineering Journal 223 (2013) 578 – 583.

[6] A. Perazzo, G. Tomaiuolo, L. Sicignano, G. Toscano, R. E. Meadows, S. P. Nolan, S. Guido, A microfluidic approach for flexible and efficient operation of a cross-coupling reactive flow, RSC Adv. 5 (2015) 63786–63792.

[7] S. Falß, G. Tomaiuolo, A. Perazzo, P. Hodgson, P. Yaseneva, J. Zakrzewski, S. Guido, A. Lapkin, R. Woodward, R. Meadows, A continuous process for buchwald-hartwig amination at micro-, lab-, and mesoscale using a novel reactor concept, Organic Process Research and Development 20 (2016) 558–567.

[8] D. M. Roberge, L. Ducry, N. Bieler, P. Cretton, B. Zimmermann, Microreactor technology: a revolution for the fine chemical and pharmaceutical industries?, Chemical Engineering and Technology 28 (2005) 318–323.

[9] C.-Y. Lee, W.-T. Wang, C.-C. Liu, L.-M. Fu, Passive mixers in microfluidic systems: a review, Chemical Engineering Journal 288 (2016) 146 – 160.

[10] A. Fani, S. Camarri, M. V. Salvetti, Investigation of the steady engulfment regime in a three-dimensional T-mixer, Physics of Fluids 25 (2013).

[11] T. Andreussi, C. Galletti, R. Mauri, S. Camarri, M. V. Salvetti, Flow regimes in T-shaped micro-mixers, Computers and Chemical Engineering 76 (2015) 150–159.

[12] R. J. Poole, M. Alfateh, A. P. Gauntlett, Bifurcation in a T-channel junction: Effects of aspect ratio and shear-thinning, Chemical Engineering Science 104 (2013) 839–848.

[13] A. Soleymani, H. Yousefi, I. Turunen, Dimensionless number for identification of flow patterns inside a T-micromixer, Chemical Engineering Science 63 (2008) 5291–5297.

[14] C. Galletti, G. Arcolini, E. Brunazzi, R. Mauri, Mixing of binary fluids with composition-dependent viscosity in a T-shaped micro-device, Chemical Engineering Science 123 (2015) 300–310.

[15] M. Engler, N. Kockmann, T. Kiefer, P. Woias, Numerical and experimental investigations on liquid mixing in static micromixers, Chemical Engineering Journal 101 (2004) 315–322.

[16] M. Hoffmann, M. Schlüter, N. Räbiger, Experimental investigation of liquid-liquid mixing in T-shaped micro-mixers using micro-LIF and micro-PIV, Chemical Engineering Science 61 (2006) 2968–2976.

[17] N. A. Mouheb, D. Malsch, A. Montillet, C. Solliec, T. Henkel, Numerical and experimental investigations of mixing in T-shaped and cross-shaped micromixers, Chemical Engineering Science 68 (2012) 278 – 289.

[18] N. Kockmann, C. Föll, P. Woias, Flow regimes and mass transfer characteristics in static micro mixers, volume 4982, 2003, pp. 319–329.

[19] D. Bothe, C. Stemich, H.-J. Warnecke, Fluid mixing in a T-shaped micromixer, Chemical Engineering Science 61 (2006) 2950–2958.

[20] S. Dreher, N. Kockmann, P. Woias, Characterization of laminar transient flow regimes and mixing in T-shaped micromixers, Heat Transfer Engineering 30 (2009) 91–100.

[21] A. Fani, S. Camarri, M. V. Salvetti, Unsteady asymmetric engulfment regime in a T-mixer, Physics of Fluids 26 (2014).

[22] A. V. Minakov, V. Y. Rudyak, A. A. Gavrilov, A. A. Dekterev, Mixing in a T-shaped micromixer at moderate Reynolds numbers, Thermophysics and Aeromechanics 19 (2012) 385–395.

[23] A. Minakov, V. Rudyak, A. Dekterev, A. Gavrilov, Investigation of slip boundary conditions in the T-shaped microchannel, International Journal of Heat and Fluid Flow 43 (2013) 161–169.

[24] C. Galletti, E. Brunazzi, R. Mauri, Unsteady mixing of binary liquid mixtures with composition-dependent viscosity, Chemical Engineering Science 164 (2017) 333–343.

[25] S. Thomas, T. Ameel, J. Guilkey, Mixing kinematics of moderate reynolds number flows in a T-channel, Physics of Fluids 22 (2010) 1–10.

[26] S. Thomas, T. Ameel, An experimental investigation of moderate reynolds number flow in a T-channel, Experiments in Fluids 49 (2010) 1231–1245.

[27] J. D. Houghton, G. A. F. Hendry, Natural food colorants, Springer US 2nd ed. (1996).

[28] P. F. Fischer, J. W. Lottes, S. G. Kerkemeier, nek5000 web page, Web page: http://nek5000. mcs. anl. gov (2008).

[29] C. Galletti, E. Brunazzi, L. Siconolfi, D. Spaltro, R. Mauri, Mixing performance of arrow-shaped micro-devices, Chemical Engineering Transactions 57 (2017) 1309–1314.

[30] C. Galletti, M. Roudgar, E. Brunazzi, R. Mauri, Effect of inlet conditions on the engulfment pattern in a T-shaped micro-mixer, Chemical Engineering Journal 185-186 (2012) 300–313.

[31] C. Galletti, E. Brunazzi, R. Mauri, Effect of composition-dependent viscosity of liquids on the performance of micro-mixers, Chemical Engineering Transactions 43 (2015) 1645–1650.

[32] J. Jeong, F. Hussain, On the identification of a vortex, Journal of Fluid Mechanics 285 (1995) 6994.

[33] N. Kockmann, T. Kiefer, M. Engler, P. Woias, Convective mixing and chemical reactions in microchannels with high flow rates, Sensors and Actuators B: Chemical 117 (2006) 495 – 508.

List of Figures

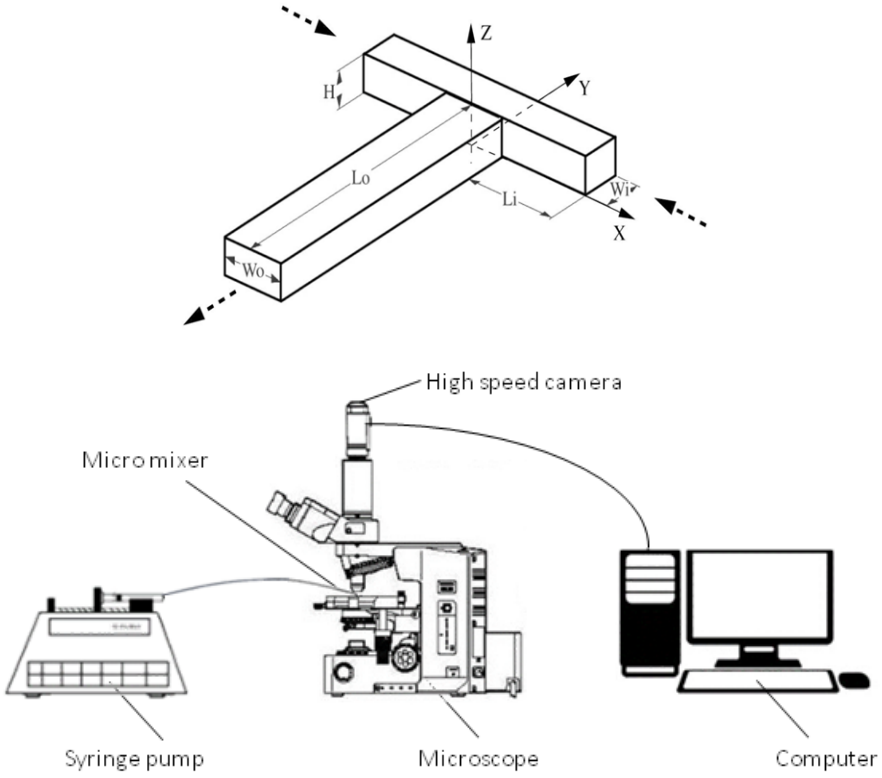

Figure 1: (a) T-mixer geometry; (b) sketch of the experimental setup.

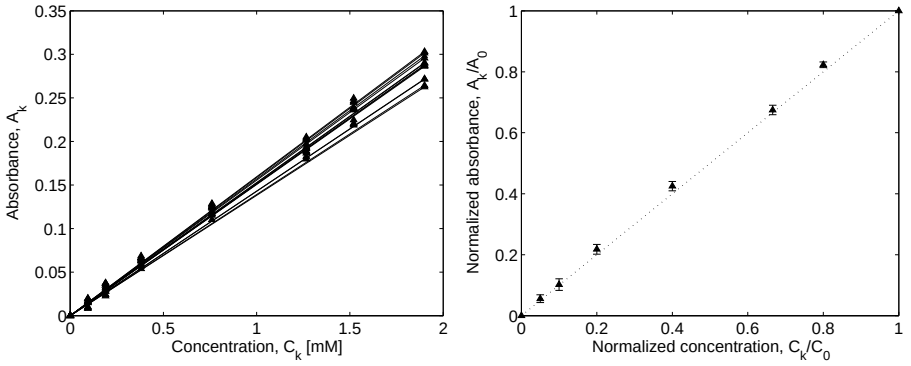

Figure 2: (a) Absorbance versus concentration obtained for 10 different pixels. (b) Normalized average absorbance versus normalized concentration. Error bars are estimated from the standard deviation of all pixels.

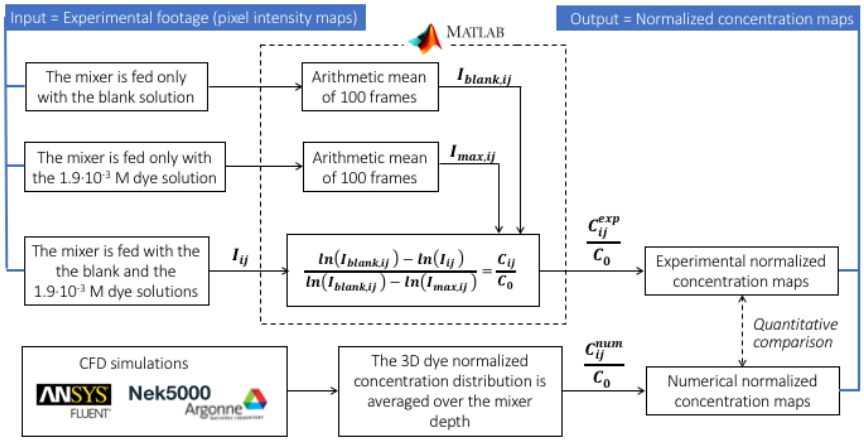

Figure 3: Flow chart of the experimental image analysis and CFD post-processing procedures.

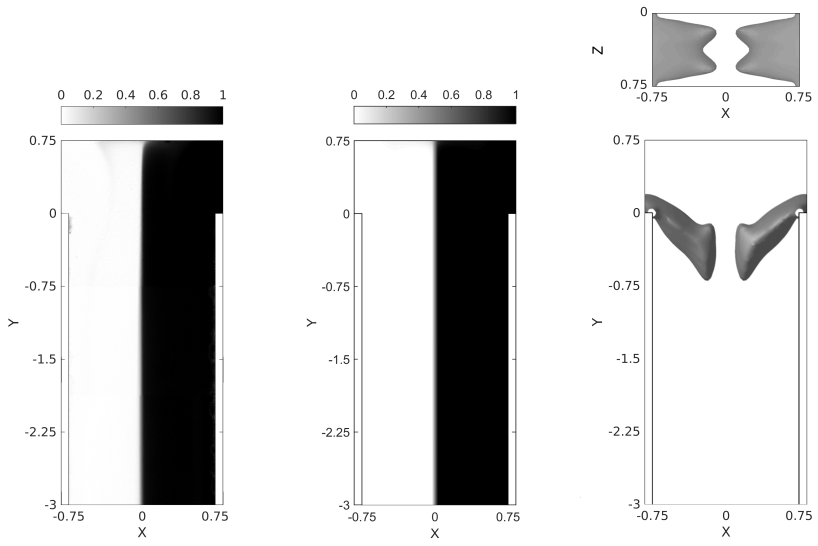

(a) (b) (c)

Figure 4: Experimental (a) and CFD (b) dye concentration fields and isosurface of the λ_2 vortex indicator (c) at $Re = 50$. Fluent simulations.

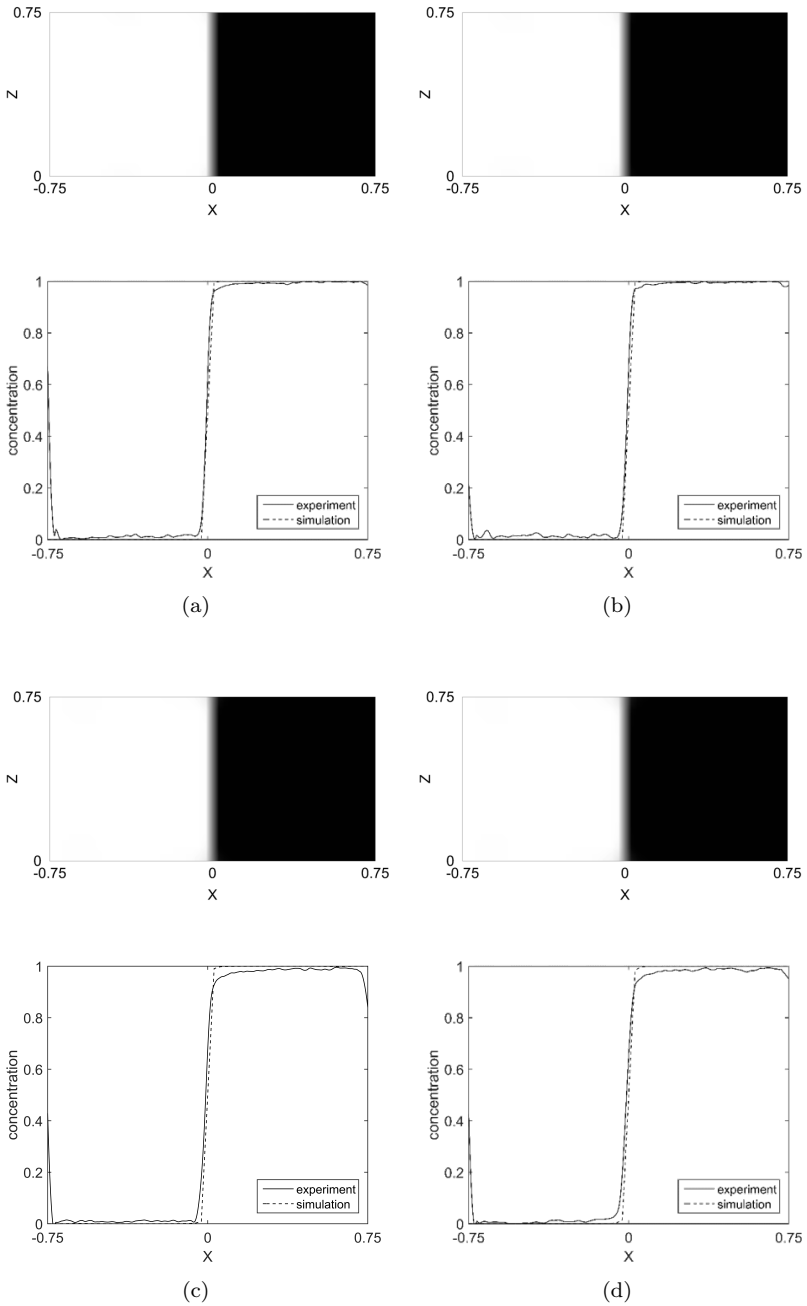

Figure 5: Dye distribution predicted through CFD (top) and comparison between experimental and CFD averaged concentration (bottom) for $Re = 50$ at different cross sections in the mixing channel: (a) $Y = -0.15$; (b) $Y = -0.45$; (c) $Y = -1.3$; (d) $Y = -2.4$. Fluent simulations.

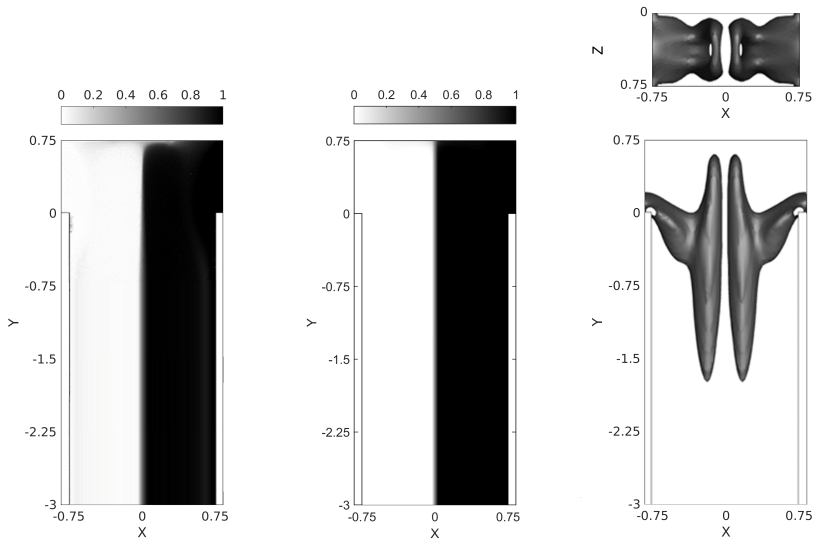

(a) (b) (c)

Figure 6: Experimental (a) and CFD (b) dye concentration fields and isosurface of the λ_2 vortex indicator (c) at $Re = 120$. Fluent simulations.

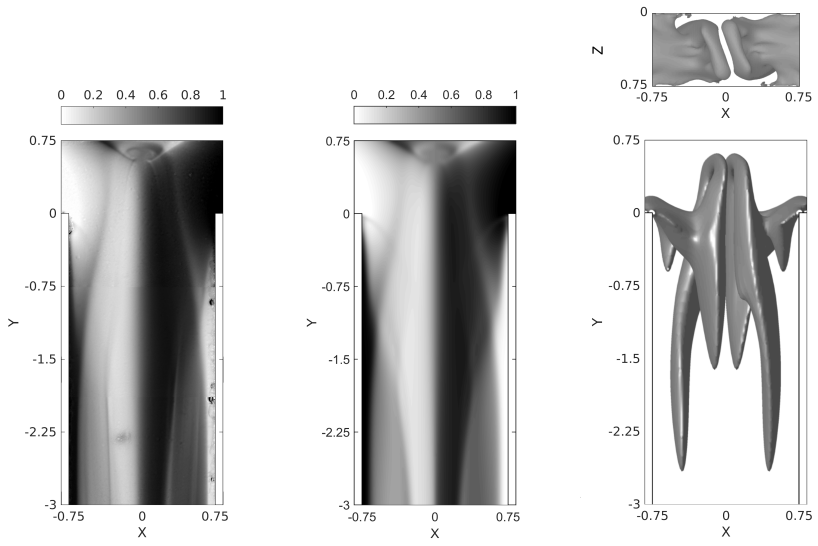

(a) (b) (c)

Figure 7: Experimental (a) and CFD (b) dye concentration fields and isosurface of the λ_2 vortex indicator (c) at $Re = 160$. Fluent simulations.

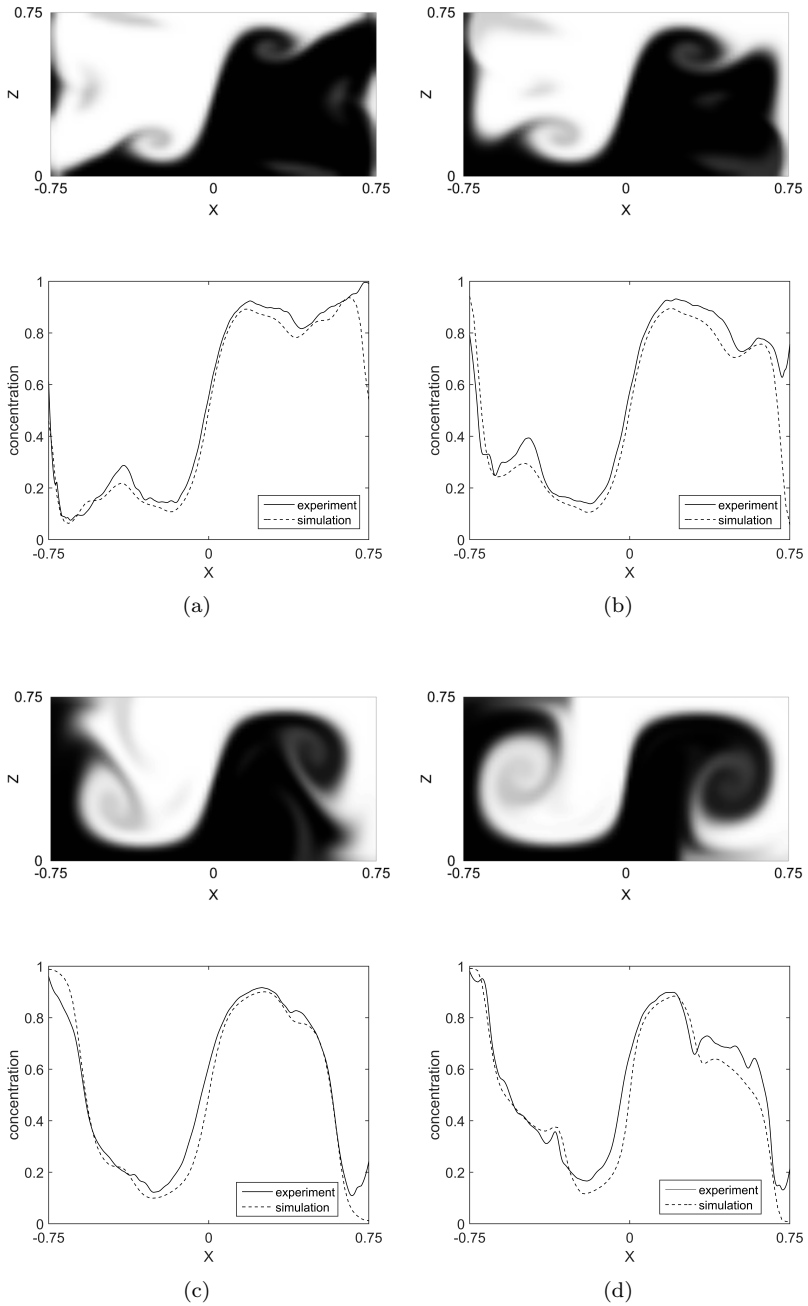

Figure 8: Dye distribution predicted through CFD (top) and comparison between experimental and CFD averaged concentration (bottom) for $Re = 160$ at different cross sections in the mixing channel: (a) $Y = -0.15$; (b) $Y = -0.45$; (c) $Y = -1.3$; (d) $Y = -2.4$. Fluent simulations.

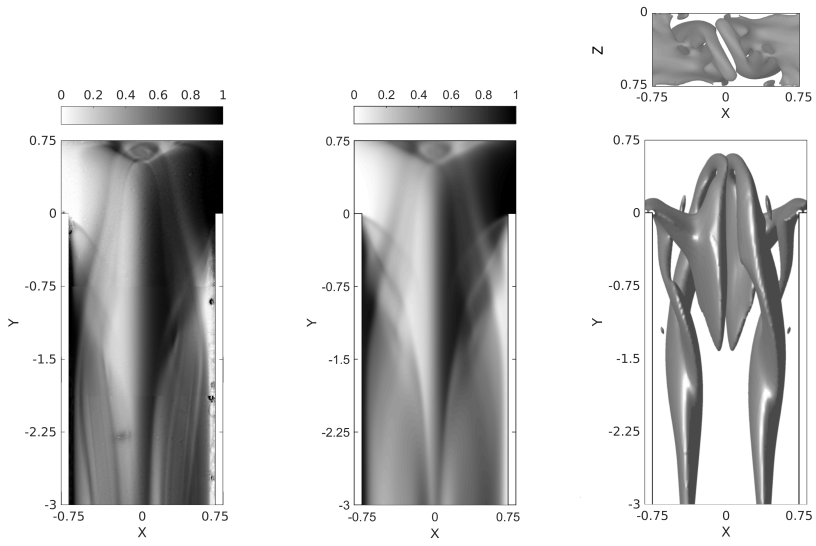

Figure 9: Experimental (a) and CFD (b) dye concentration fields and isosurface of the λ_2 vortex indicator (c) at $Re = 200$. Fluent simulations.

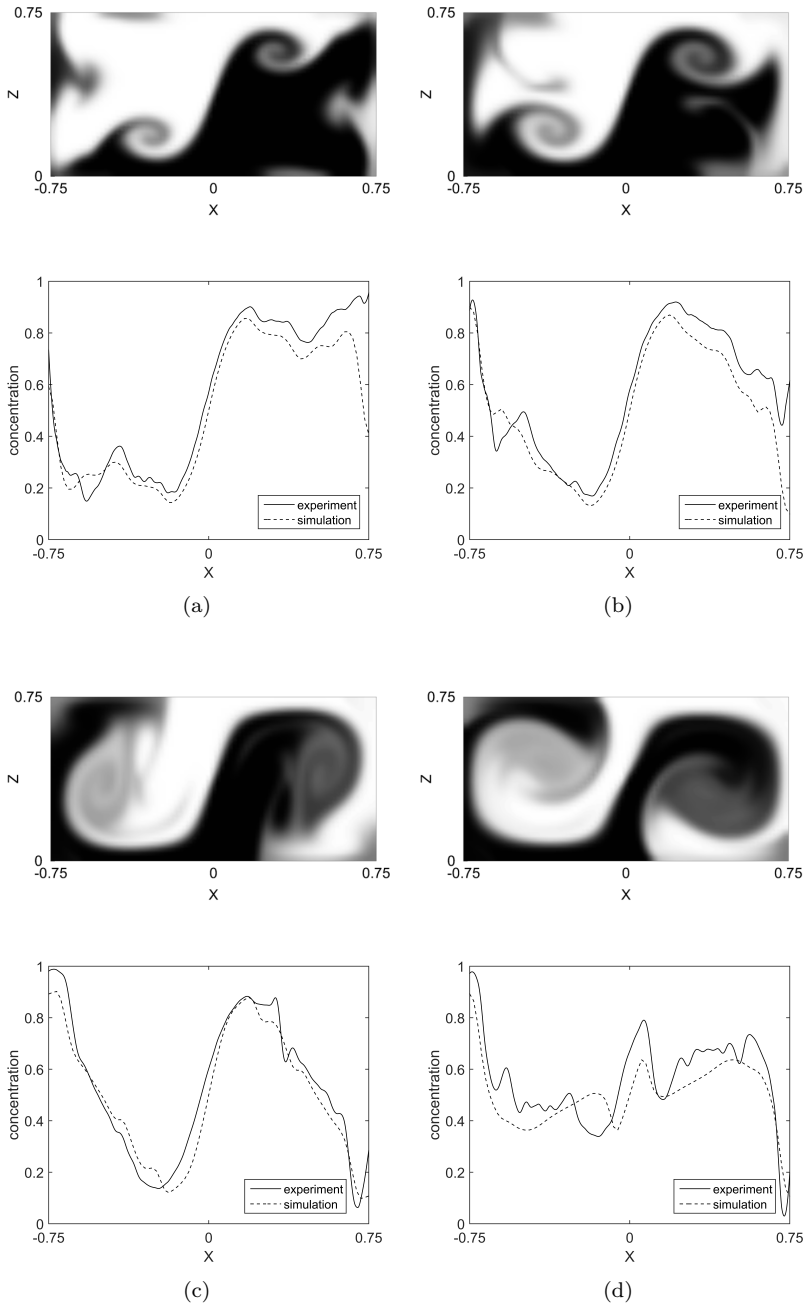

Figure 10: Dye distribution predicted through CFD and comparison between experimental and CFD averaged concentration for $Re = 200$ at different cross sections in the mixing channel: (a) $Y = -0.15$; (b) $Y = -0.45$; (c) $Y = -1.3$; (d) $Y = -2.4$. Fluent simulations.

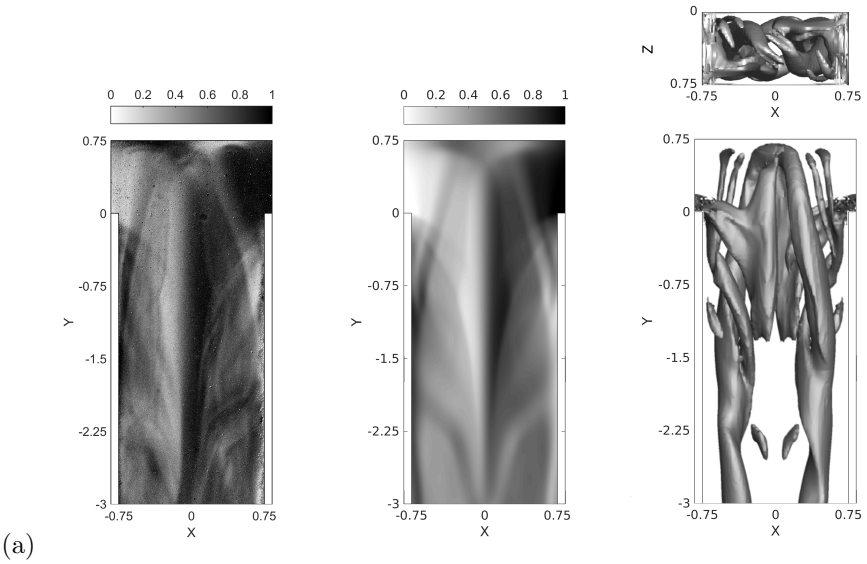
0 0.2 0.4 0.6 0.8 1
0.75
0
-0.75
-1.5
-2.25
-3
Y
-0.75 0 0.75
X
0
0.75
Z

(a)

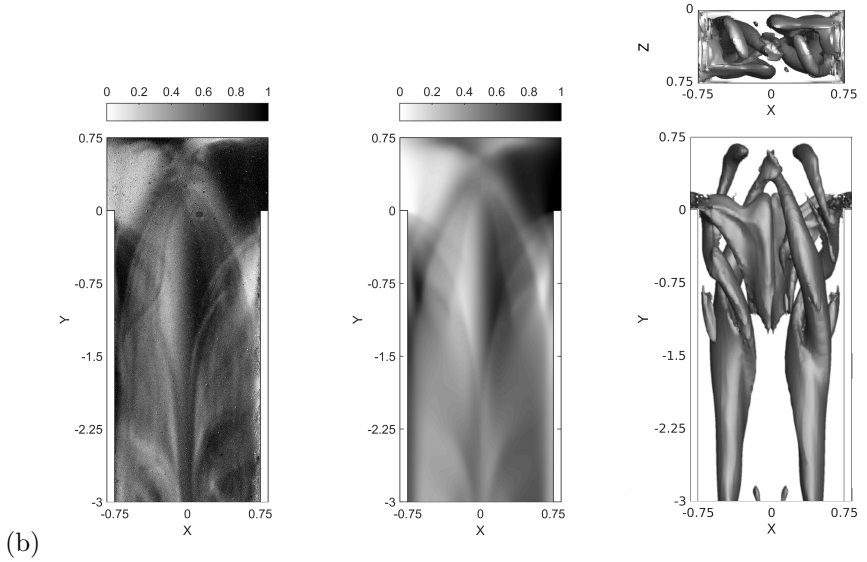
0 0.2 0.4 0.6 0.8 1
0.75
0
-0.75
-1.5
-2.25
-3
Y
-0.75 0 0.75
X
0
0.75
Z

(b)

Figure 11

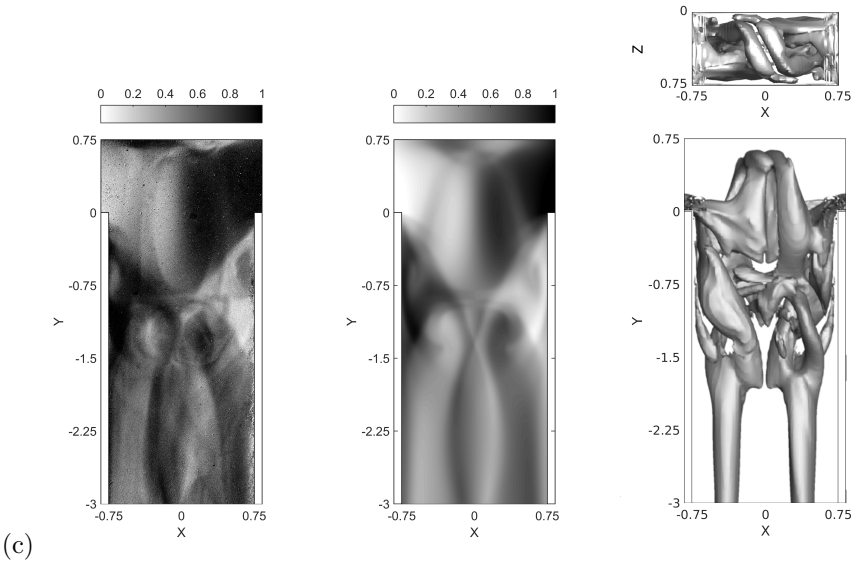

(c)

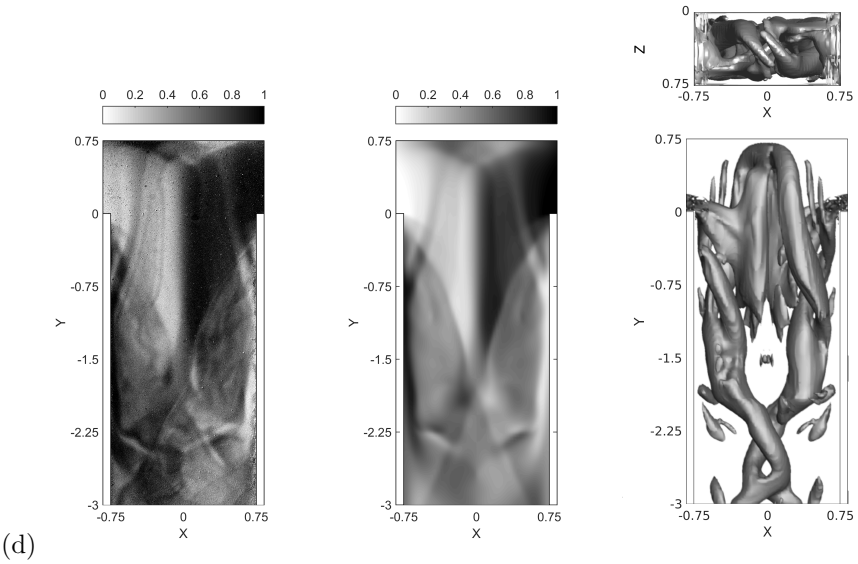

(d)

Figure 11: Experimental (left) and CFD (middle) dye concentration fields and isosurface of the λ_2 vortex indicator (right) at $Re = 280$ and different times: (a) $\frac{t}{\tau} = 0$; (b) $\frac{t}{\tau} = 0.25$;(c) $\frac{t}{\tau} = 0.5$;(d) $\frac{t}{\tau} = 0.75$. NEK5000 simulations.

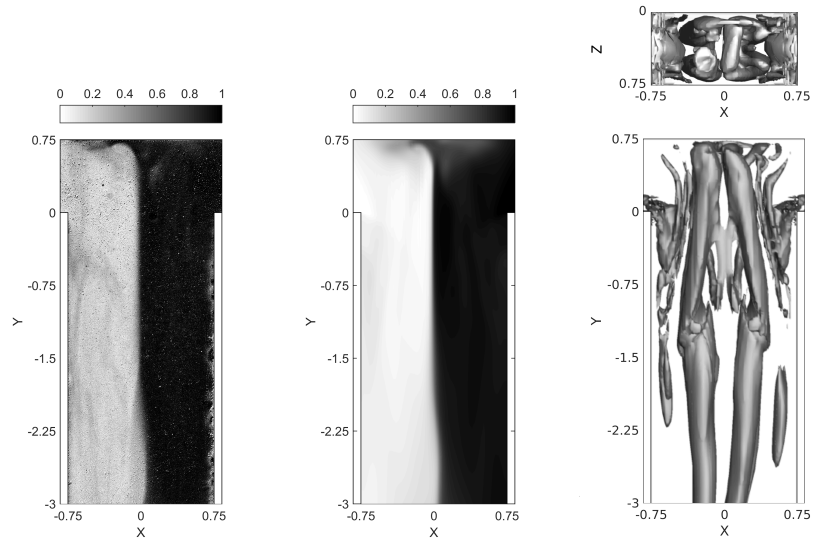
0 0.2 0.4 0.6 0.8 1
0.75
0
-0.75
-1.5
-2.25
-3
Y
-0.75 0 0.75
X
0
0.75
Z

(a)

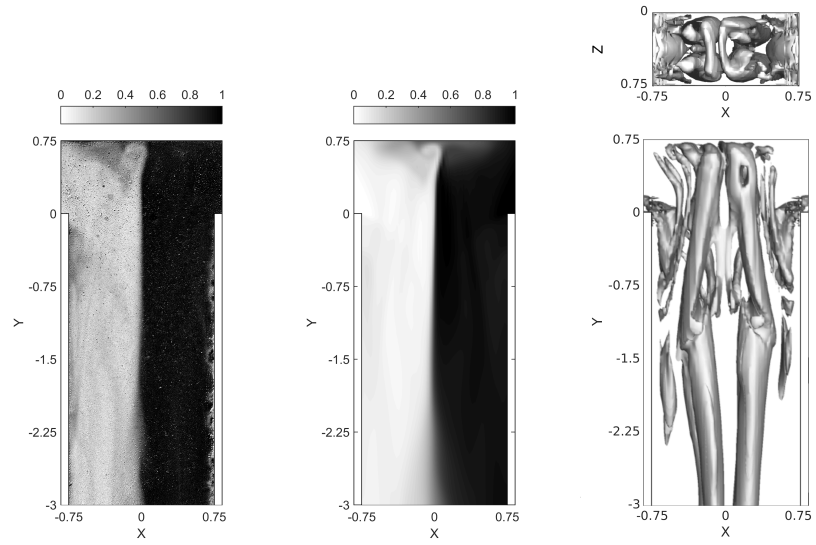
0 0.2 0.4 0.6 0.8 1
0.75
0
-0.75
-1.5
-2.25
-3
Y
-0.75 0 0.75
X
0
0.75
Z

(b)

Figure 12

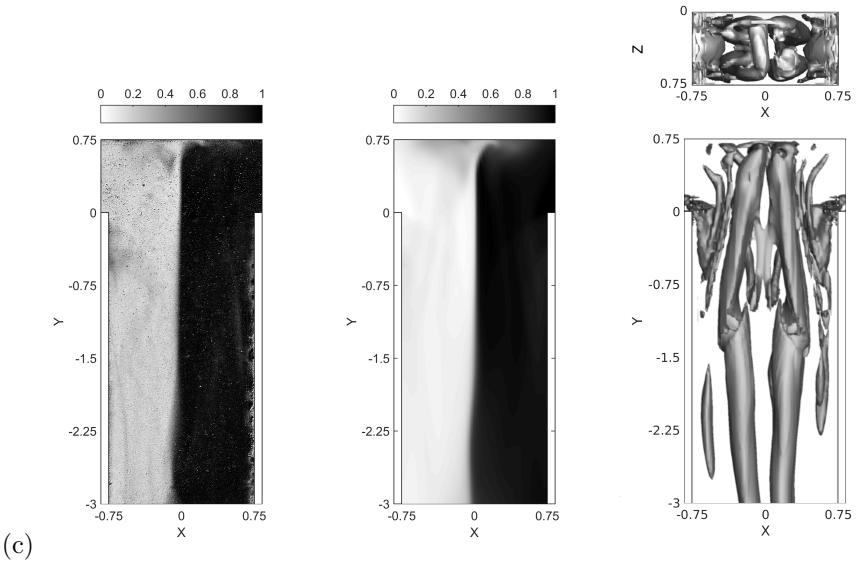

(c)

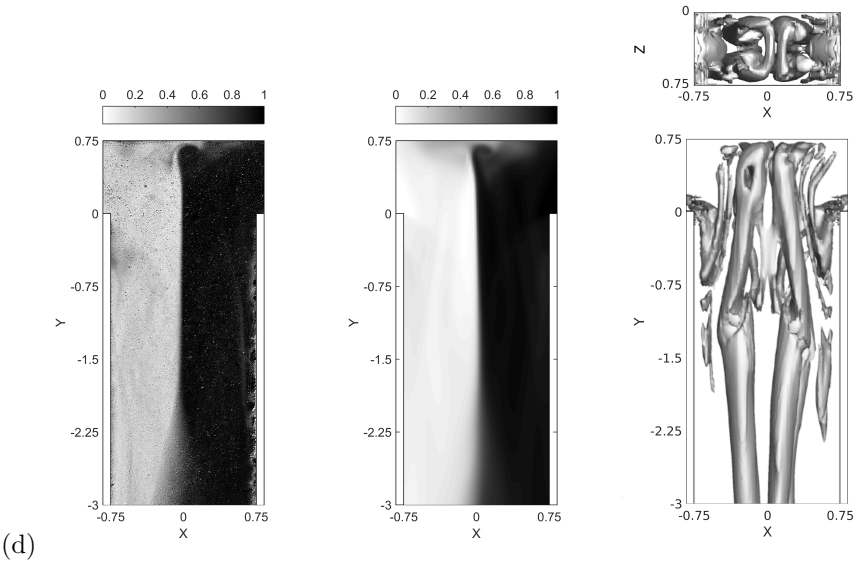

(d)

Figure 12: Experimental (left) and CFD (middle) dye concentration fields and isosurface of the λ_2 vortex indicator (right) at $Re = 450$ and different times: (a) $\frac{t}{\tau} = 0$; (b) $\frac{t}{\tau} = 0.25$;(c) $\frac{t}{\tau} = 0.5$;(d) $\frac{t}{\tau} = 0.75$. NEK5000 simulations.

List of Tables

Table 1: Summary of the flow regimes as from the experimental images and predicted iso-surfaces of the λ_2 vortex indicator. For the unsteady regimes snapshots refer to $\frac{t}{\tau} = 0$ and $\frac{t}{\tau} = 0.5$.

Flow regime	Flow visualization	Vortical structures
Stratified regime ($Re < 80$)	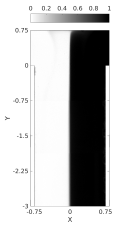	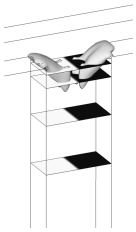
Vortex regime ($Re = 80 \div 140$)	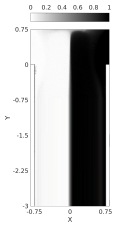	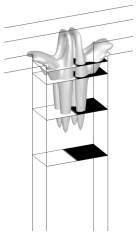
Engulfment regime ($Re = 145 \div 220$)	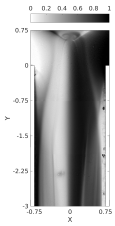	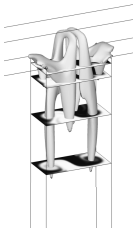
Unsteady periodic asymmetric regime ($Re = 225 \div 320$)	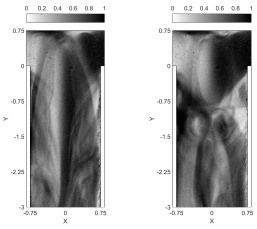	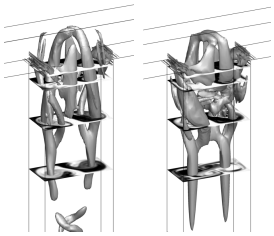
Unsteady periodic symmetric regime ($Re = 325 \div 510$)